Studies in Applied Mathematics

WILEY

STUDIES IN APPLIED MATHEMATICS

SPECIAL ISSUE ARTICLE OPEN ACCESS

Advances in the Mathematics and Physics of Solitons in Memory of David Kaup

Numerical Approaches in Nonlinear Fourier Transform-Based Signal Processing for Telecommunications

Egor Sedov[1] | Igor Chekhovskoy[2] | Mikhail Fedoruk[2] | Sergey Turitsyn[1]

[1]Aston Institute of Photonic Technologies, Aston University, Birmingham, UK | [2]Laboratory of Nonlinear Photonics, Novosibirsk State University, Novosibirsk, Russia

Correspondence: Egor Sedov (egor.sedoff@gmail.com)

Received: 28 April 2024 | **Revised:** 12 November 2024 | **Accepted:** 13 November 2024

Funding: This work was supported by the Russian Science Foundation (project no. 20-11-20040) and Engineering and Physical Sciences Research Council (EPSRC) project TRANSNET.

Keywords: inverse scattering transform | nonlinear Fourier transform | nonlinear Schrödinger equation | optical communication

ABSTRACT

We discuss applications of the inverse scattering transform, also known as the nonlinear Fourier transform (NFT) in telecommunications, both for nonlinear optical fiber communication channel equalization and time-domain signal processing techniques. Our main focus is on the challenges and recent progress in the development of efficient numerical algorithms and approaches to NFT implementation.

1 | Introduction

Nonlinear Schrödinger equation (NLSE) is one of the key master models in nonlinear science, that is highly important in various areas of physics and practical engineering applications, such as nonlinear optics, hydrodynamics, plasma physics, physics of atmosphere, biophysics, field theory, and many others (see, e.g., [1–15] and references therein). This mathematical model is generic, being based on rather general assumptions about media nonlinearity and dispersion (or diffraction in the spatial waves context). Our focus in this work will be on the high-speed optical communications [6–8], therefore, without loss of generality, we consider here NLSE in the fiber-optic context, with Z being the evolution coordinate along the fiber link and a field (signal) being a function of time T. The basic NLSE model governing the propagation of a slowly varying optical field envelope $A(T,Z)$ for a single-polarization signal in the cascaded fiber-optic transmission system reads (see for details, e.g., [6–8]):

$$i\frac{\partial A}{\partial Z}-\frac{\beta_2}{2}\frac{\partial^2 A}{\partial T^2}+\gamma|A|^2A=iG(Z)A, \tag{1}$$

where Z is the distance along the fiber link, T is retarded time, β_2 is the group velocity dispersion parameter, γ is the nonlinear coefficient, and $G(Z)$ is a periodic function describing fiber loss and periodic amplification to compensate for the signal attenuation. For instance, in the case of the point-action (lumped) Erbium-doped fiber amplifiers, the periodic (with the period Z_a—distance between amplifiers) function $G(z)$ can be written just as: $G(Z)=-\alpha/2+(\exp[\alpha Z_a/2]-1)\times\sum_{n=1}^{N}\delta(z-nZ_a)$. Thus, the signal amplitude (power) is boosted to the initial level after each amplifier span. After transform $A(T,Z)=\exp[\int_0^Z G(z')dz']B(T,Z)$, which in the case of point-action amplifiers is equal to $\exp(-\alpha Z/2)B(T,Z)$, in between two amplifiers and under certain conditions (see for details, e.g., [6, 7, 16–18]) Equation (1), with loss and gain, can be approximated on average by the lossless NLSE ($G(Z)=0$) on the distance scales larger than the amplification period. We would like to point out that the lossless NLSE considered below is just an approximate model that becomes less accurate when next order terms, such as, for example, optical noise, high-order dispersion, and nonlinear Raman effect become important, or when the path-average condition becomes nonvalid (e.g., with an increase of signal power level)

(see, e.g., [5–7, 17]). It should also be noted that lossless NLSE can be used as good model of real fiber-optic transmission systems with special design using Raman amplification in ultra-long fiber lasers [16, 19] or based on dispersion-decreasing fibers [20].

We consider, without loss of generality, point-action amplification. Averaging (1) over one amplifier span, yields for the field $U(T,Z) = \langle B(T,Z)\rangle = \int_0^{L_{sp}} dZB(T,Z)/L_{sp}$, the lossless NLSE model in the leading order. We also add its dimensionless representation that will be used below:

$$\frac{\partial U}{\partial Z} = -i\frac{\beta_2}{2}\frac{\partial^2 U}{\partial T^2} + i\frac{G_0-1}{\log G_0}\gamma|U|^2U \quad \xRightarrow[\text{dimensionless}]{} \quad i\frac{\partial q}{\partial z} + \frac{\sigma}{2}\frac{\partial^2 q}{\partial t^2} + |q|^2 q = 0. \tag{2}$$

Here, $G_0 = \exp[\alpha L_{sp}]$. This equation is a normalized (path-averaged over an amplification period) NLSE that will be used throughout the paper. Here, the normalization is introduced in a standard manner: dimensionless time $t = T/T_0$ and distance $z = Z/L_D$, with T_0 being some characteristic time scale (e.g., symbol interval), dispersion length $L_D = T_0^2/|\beta_2|$, and characteristic power $P_0 = \log G_0/(\gamma L_D(G_0-1))$. The dimensionless complex field $q(t,z) = U(T,Z)/\sqrt{P_0}$. The parameter $\sigma = \text{sign}(-\beta_2\gamma)$ denotes either anomalous (focusing, $\sigma = 1$) or normal (de-focusing, $\sigma = -1$) dispersion. We consider here the case of the anomalous dispersion $\beta_2 < 0$ ($\sigma = 1$), when general solutions of this equation can include both the dispersive (linear-like) waves and the coherent localized (in time) structures—solitons [8]. Any initial signal evolving according to this master model can be presented as a nonlinear superposition of dispersive waves and soliton(s). Note that the availability of a free parameter T_0 in the normalization allows to manipulate and control nonlinear spectrum (defined below) of the real-world signal.

The NLSE belongs to the class of the so-called integrable nonlinear partial differential equations (PDEs) that can be integrated by the inverse scattering transform (IST) method developed for this equation by Zakharov and Shabat [4], also known as the nonlinear Fourier transform (NFT) [21, 22]. With the understanding that in this special issue this might be redundant information, we still would like to outline the well-known basics of IST/NFT for readers who might not be experts in the field. The NFT allows to present the optical signal through its nonlinear spectrum. This spectrum is determined by the solutions to the Zakharov–Shabat problem (ZSP). First step is to compute the nonlinear spectrum of the signal at the transmitter $q(t, z = 0) = q_0(t)$, the problem is laid out as

$$\begin{cases} -\dfrac{\partial \psi_1}{\partial t} + q_0(t)\psi_2 = i\zeta\psi_1, \\ \dfrac{\partial \psi_2}{\partial t} + q_0^*(t)\psi_1 = i\zeta\psi_2. \end{cases} \tag{3}$$

The input signal $q_0(t)$ plays the role of a potential, and $\zeta = \xi + i\eta$ is a complex parameter—analog of frequency in Fourier domain. When the signal $q_0(t)$ is well localized (decays fast enough as $|t|$ approaches ∞), one can introduce the scattering coefficients $a(\zeta) = \lim_{t\to-\infty} \psi_1(t,\zeta)e^{i\zeta t}$ and $b(\zeta) = \lim_{t\to-\infty} \psi_2(t,\zeta)e^{-i\zeta t}$ (see for details, [4, 21]). These coefficients satisfy the following condition when the spectral parameter is real: $|a(\xi)|^2 + |b(\xi)|^2 \equiv 1$. Full spectral data of the ZSP are given by $a(\zeta)$ and $b(\zeta)$ and consist of two parts: continuous and discrete. Continuous part always present and can be represented by $b(\xi)$, usually called b-coefficient, or, more commonly, using reflection coefficient $r(\xi) = b(\xi)/a(\xi)$, $\xi \in \mathbb{R}$. In the limit case, when the average signal amplitude tends to zero ($q_0(t) \to 0$), $r(\xi)$ converges to the linear Fourier spectrum of the signal. The second part—discrete—is not always present in the (nonlinear Fourier) NF spectrum. The coefficient $a(\xi)$ can be analytically continued to the upper half of the ζ-plane as a function $a(\zeta)$, which has simple zeros at the eigenvalue points, $a(\zeta_n) = 0$ (excluding the degenerate case where an eigenvalue point is a multiple zero). In addition to the real line $\zeta = \xi$, the coefficient b is generally defined only at the eigenvalue points ζ_n. For exponentially decreasing signals, which contain all signals of interest in a communications setup, b is analytic in a strip around the real axis whose width depends on the decay constant (see [21, p. 268]). However, it can be analytically continued to the entire upper half-plane if the potential $q_0(t)$ has a compact support. The zeros of $a(\zeta) = 0$ in the upper half-plane give us the discrete spectrum $\{\zeta_k\}, k = 1, K$, with the phase coefficients defined by $r_k = \frac{b(\zeta_k)}{a'(\zeta_k)}\Big|_{\zeta=\zeta_k}$, where $a'(\zeta) = \frac{da(\zeta)}{d\zeta}$. The discrete spectrum corresponds to the soliton component of the signal. The NFT allows one to find the evolution (with z) of the signal $q(t,z)$ described by the NLSE channel by solving two linear problems instead of solving the nonlinear PDE. A complex signal evolution governed by NLSE is replaced by three steps:

1. forward (or direct) transform from $q(t, z = 0)$ to the nonlinear scattering data of the initial signal that can be represented as $\Sigma(0,t)$ (see below),
2. trivial evolution of the nonlinear spectrum with z, and
3. inverse transform to restore signal $q(t,z)$ at any desired propagation distance z from the evolved nonlinear spectrum $\Sigma(z,t)$.

It is seen from above that the NFT method is similar to the standard Fourier approach for the solution of linear evolution equations: present initial field in the spectral domain, consider trivial evolution of each spectral harmonic, and reconstruct evolved signal from the spectral components known for any propagation distance. The NFT can be used for both solving nonlinear PDEs and enabling the decomposition of complex wave fields into simpler components to facilitate analysis.

As we previously discussed, the main "power" of NFT is the trivial evolution of spectral data with distance z. The way scattering data changes with the distance is $r(\xi,z)=r(\xi)\mathrm{e}^{-2i\xi^2 z}$ and $r_k(z)=r_k\mathrm{e}^{-2i\zeta_k^2 z}$. So, knowledge of information about the full NF spectrum, reflection coefficient, discrete spectrum, and its phase coefficients, gives us all information about the evolution of the signal with distance in the nonlinear spectral domain. The scattering data combine into the core $\Sigma(z,t)$, which is a sum of the discrete and continuous parts of the nonlinear spectrum:

$$\begin{aligned}\Sigma(z,t)&=\Sigma_c(z,t)+\Sigma_d(z,t)\\&=\frac{1}{2\pi}\int_{-\infty}^{+\infty}d\xi r(\xi,z)\mathrm{e}^{-i\xi t}-i\sum_{k=1}^{K}r_k(z)\mathrm{e}^{-i\zeta_k t}.\end{aligned}\tag{4}$$

Here, K represents the total number of discrete eigenvalues in the signal.

The last part of working with the NFT involves reconstructing the signal from the scattering data. To get the signal $q(t,z)$ back at a certain distance z, we use the core $\Sigma(z,t)$ in a system of two integral equations, known as left Gelfand–Levitan–Marchenko equations (GLME):

$$\begin{aligned}&\Theta_1^*(t,s)+\int_{-s}^{t}\Sigma(s+\tau)\Theta_2(t,\tau)d\tau=0\quad\text{and}\\&-\Theta_2^*(t,s)+\int_{-s}^{t}\Sigma(s+\tau)\Theta_1(t,\tau)d\tau+\Sigma(t+s)=0,\end{aligned}\tag{5}$$

where $-t\le s<t$ and $0\le t\le T$, with $\Sigma(t)\equiv\Sigma(z,t)$ already in desired spatial point z. We need to determine two functions, Θ_1 and Θ_2 as solutions of these equations. Once these functions are found, we can recover the signal using the straightforward formula: $q(t)|_z=-2\Theta_2^*(t,t)$.

There is an infinite number of conservation laws that connect NLSE integrals of motion with the corresponding scattering data. It is useful to remind the so-called Parseval equality for NLSE, which can be used to control the accuracy of numerical solutions by checking the balance between continuous and discrete spectral energies:

$$\begin{aligned}&E_c=-\frac{1}{\pi}\int_{-\infty}^{+\infty}\ln\,|a(\xi)|^2d\xi=\frac{1}{\pi}\int_{-\infty}^{+\infty}\ln\left(1+|r(\xi)|^2\right)d\xi,\\&E_d=\sum_{k=1}^{K}2i\left(\zeta_k^*-\zeta_k\right)=4\sum_{k=1}^{K}\eta_k,\end{aligned}\tag{6}$$

where E_c and E_d represent the energy of the continuous and discrete spectrum, respectively. The sum of these energies gives the total energy, which is equivalent to the signal energy in the time domain: $E=E_c+E_d$.

In the context of nonlinear fiber channels, the NFT is used not as a tool for the NLSE solution, but as a signal processing method [18, 23]. This concept originated from the work of Hasegawa and Nyu [24], who proposed to use the nonlinear spectrum (the so-called eigenvalues) for the data modulation and transmission. This was a remarkable departure from the idea of exploiting the time-domain soliton in on–off (soliton—logical one, no soliton—logical zero) keying binary direct detection transmission [8]. Over the past decades, the NFT-based optical transmission techniques have been resurrected and greatly extended (see, e.g., [18, 23] and references therein). When the optical field propagates down the ideal NLSE channel, the evolution of the nonlinear modes inside the NF domain is trivial, in contrast to the complex nonlinear evolution of signal in the space–time domain. Because of this property, we can theoretically get rid (or reduce them) of the infamous nonlinear cross-talk degrading the transmission performance at high signal powers [25]. However, of course, this is possible only for pure NLSE channels. In real optical fiber systems, the NLSE model has limited application [6, 7, 17], as the signal is affected by deviations from the lossless model, optical noise, higher-order effects, and other factors. The NLSE channel is only an approximation of the real fiber-optic links, either in the path-average regime [6, 7, 17] or quasi-lossless links [16, 19, 26], where attenuation is compensated by the specially designed distributed Raman amplification. Note that as a signal processing tool, NFT can be applied to nonintegrable, including dissipative systems (see, e.g., [27–32] and references therein). We would like to stress, that in this work we do not use coding over eigenvalues as in [24], our focus is to study how IST/NFT can help to process of the conventional telecommunication signals used in the modern coherent detection transmission links. As most of the installed fiber-optic links use standard monomode fiber, we focus here on nonlinear transmission modes in the case of anomalous dispersion. Applications and limitations of NFT application in the case of normal dispersion were investigated in [33–36].

We do not aim here at the comprehensive overview of all recently developed techniques and approaches to applications of NFT in optical communications. However, we mention few methods relevant to our discussion of the numerical methods below: nonlinear inverse synthesis scheme proposed in [37, 38] allows on to deal only with the continuous spectrum using conventional telecommunication signals; nonlinear frequency division multiplexing with continuous spectrum was studied in [39–41]; transmission based on discrete spectrum has been examined in [42–44]; both with the discrete and the continuous spectrum was utilized in [45]; and nonlinear frequency division multiplexing with b-modulation was proposed and studied in [46–48].

2 | Basics of IST/NFT Application in Optical Communications

We will consider IST/NFT applications in a single spectral channel. Even though, this is not directly relevant to this work, for the readers unfamiliar with optical communications, we briefly mention that signal can be transmitted in several frequency channels—the so-called wavelength-division-multiplexing (WDM) technique. WDM is a widely used and crucial technology in optical communications, enabling the simultaneous transmission of multiple signals along the same fiber-optic cable, each at an own wavelength. Multiple carrier frequencies (wavelengths) in the same channel spectral channel also can be used, for instance, in the so-called optical frequency division multiplexing (OFDM). In OFDM, data are split across multiple orthogonal subcarriers within the same spectral

channel. In telecommunication applications, it is common to deal with the equations written in the real-world units related to the transmission system and signal parameters, such as, for example, carrier light frequency, average signal power, and so on. However, in this paper, we will use both dimensional and dimensionless equations, because all the NFT analysis is performed with dimensionless signals. Of course, the conversion from real-world units to normalized form and back can be easily done using the formulas from the introduction section. The optical signal for WDM/OFDM transmission is represented as a superposition of modulated signals, each associated with a distinct wavelength or frequency, $A(T, Z = 0) = A_{in}(T)$ and $q(t, z = 0) = q_{in}(t)$ are given by:

$$A_{in}(T) = \sqrt{P_0} \sum_{j=1}^{J} \sum_{n=1}^{N_c} c_{jn}\, f(T - jT_s) \mathrm{e}^{-i2\pi\nu_n T} \quad \xrightarrow[\text{dimensionless}]{} \quad q_{in}(t) = \sqrt{Q_0} \sum_{j=1}^{J} \sum_{n=1}^{N_c} c_{jn}\, \hat{f}(t - j) \mathrm{e}^{-i2\pi\hat{\nu}_n t}, \tag{7}$$

where T_s is the symbol interval, N_c is either the number of considered spectral channels (WDM case), or a number of subcarriers in the case of multicarrier signal (OFDM), J is the number of symbols in the time-domain signal stream, $\nu_n = (n - \frac{N_c+1}{2}) \cdot \Delta$, and Δ is the channel spacing; c_{jn} is the complex point from modulation constellation (symbol) of the jth symbol on the nth channel, $f(T - jT_s)$—carrier pulse shape (different for WDM and OFDM). As discussed in the paragraph following Equation (2), we introduce dimensionless time $t = T/T_0$, characteristic power $P_0 = \log G_0/(\gamma L_D(G_0 - 1))$, and the dimensionless complex field $q(t, z) = A(T, Z)/\sqrt{P_0}$. While the characteristic time interval can be chosen arbitrarily, here it is natural and convenient to choose this as the symbol interval: $T_0 = T_s$. The reader may notice that the normalization transforms the equation for A_{in} into q_{in} with a normalization factor equal to one. However, we explicitly introduce a coefficient $\sqrt{Q_0}$ to show that changing this coefficient changes the amplitude, and thus the power of the dimensionless signal. Quantities $\hat{f}$ and $\hat{\nu}_n$ correspond to the dimensionless variant of the carrier pulse and carrier frequency, respectively.

Without loss of generality, in this work we consider the so-called quadrature amplitude modulation (QAM) format, which exploits both the amplitude and phase of the light signal. QAM is a bandwidth-efficient (compared to binary coding) signaling scheme that achieves higher data rates within a given bandwidth by encoding multiple bits per symbol through the use of a constellation of amplitude and phase combinations. The number of states in QAM is 2^M, determined by the number of bits per symbol, such as in a 16-QAM system ($M = 4$) or a 64-QAM system ($M = 6$), and so on. Figure 1 shows examples of constellation diagrams for 16-QAM (left) and 64-QAM (right). These diagrams represent the standard form of QAM modulation, where different symbols are located at grid points on the complex plane. Above each point, the corresponding bit sequence for that point can be observed. All neighboring points differ from each other by only one bit, this technique is known as Gray coding [49].

On the receiver side, the incoming signal $A_{out}(T)$ is demodulated to recover the original symbols that were sent. In case of WDM, different spectral channels are demultiplexed (filtered out) and processed separately. Essentially, the received signal is processed by a matched filter in a way that isolates each transmitted symbol, denoted by b_j, using the conjugate of the pulse shape $f^*(T - jT_s)$. In the case of a single channel ($N_{ch} = 1$ in Equation 7), the received symbols b_j can be found by applying a matched filter:

$$b_j = \frac{1}{\sqrt{P_0}} \int_{\infty}^{\infty} dT \cdot A_{out}(T) \cdot f^*(T - jT_s) \quad \xrightarrow[\text{dimensionless}]{} \quad b_j = \frac{1}{\sqrt{Q_0}} \int_{\infty}^{\infty} dt \cdot q_{out}(t) \cdot \hat{f}^*(t - j). \tag{8}$$

The matched filter is an essential component in digital communication systems, utilized at the receiver to maximize the signal-to-noise ratio (SNR) for a given received signal, thereby facilitating optimal detection of symbols b_j. In an ideal, error-free transmission, these symbols should be equal to c_j. However, in practical communication channels, the received symbols b_j deviate from the transmitted ones c_j due to the impact of noise and other effects (nonlinearity in the case of fiber communications). Spectral processing can also lead to errors; for instance, for a multichannel WDM signal, we first cut the spectral interval corresponding to each channel. This isolates a part of the WDM signal, which can then be treated as a single-channel WDM to find the corresponding received symbols. The neighboring channels can affect each other during propagation through the fiber, leading to nonlinear cross-talk (spectral channels do not interact in the linear transmission regime). Evidently, to take advantage of the NFT to compensate for nonlinear distortions, we need to operate with the signal detected in the whole available bandwidth. After cutting off some spectral components using a WDM filter, we lose information about neighboring channels. Therefore, the analysis presented in this work is for a single channel (e.g., after WDM filtering). In general, NFT can also be applied to a group of WDM channels, if the receiver bandwidth allows them to be separated and processed together. The NFT approach is versatile and can be applied to different signal formats, modulations, and information coding schemes, subject of availability of the information about both amplitude and phase of the signal (coherent detection). In practical communication systems, error-correcting codes, including forward error correction (FEC), play a crucial role in ensuring reliable data transmission by detecting and correcting errors that occur during signal transmission. These coding techniques (such as, e.g., Reed–Solomon, Hamming, or LPDC codes) are

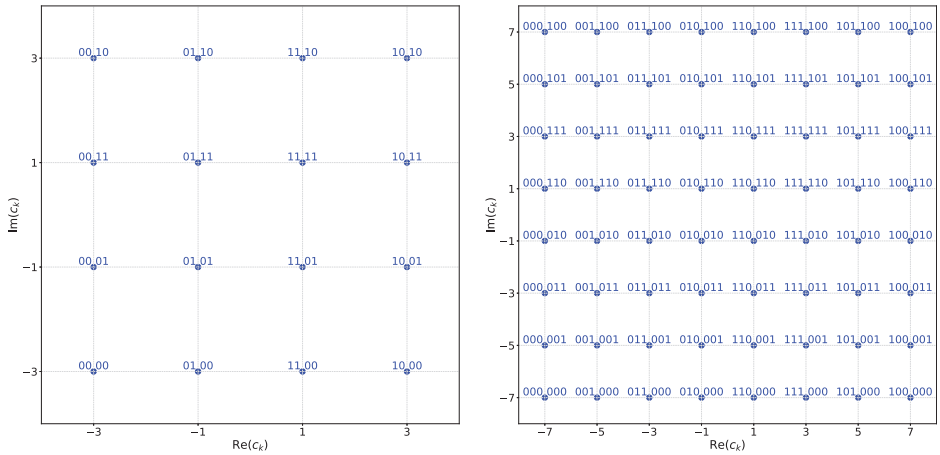

FIGURE 1 | Example of a constellation diagram for QAM. (a) 16-QAM format and (b) 64-QAM. Above each point, the corresponding bit sequence for that point is displayed. All neighboring points differ from each other by only one bit—Gray coding method.

essential for achieving high transmission quality, especially in noisy environments. While we do not examine in this work the most efficient coding and modulation schemes using NFT, but rather focus on the basic principles of such signal processing, it is important to note that coding can typically be considered in parallel to development NFT algorithms. FEC will affect estimate/evaluation of the spectral efficiency (SE) as part of the bits will be allocated to correct errors, reducing overall SE. For more information about error coding, FEC, and their application in optical communication, see references such as [50–52].

The main focus of this work is to provide examples of applications of IST/NFT in a realistic telecommunication context. Optical signal transmission is characterized by several key performance parameters. Bitrate, which is a characteristic of the digital data transmission speed in bits per second, is defined by multiplying the baud rate (symbol transmission rate per second) by the number of bits each symbol represents:

$$\text{Bitrate} = \text{Baud Rate} \times M, \tag{9}$$

where M is the number of bits per symbol. It is seen that the bitrate can be increased either by using higher baud rates (shorter symbol intervals and, respectively, shorter carrier pulses) or by encoding more bits within the symbol interval. The overall number of available degrees of freedom is proportional to the product of the channel bandwidth Ω and the total time interval over which information is sent. This leads to the SE metric:

$$\text{SE} = \frac{\text{Number of error-free transmitted bits per second}}{\text{Channel bandwidth}}. \tag{10}$$

Assessing the performance of digital signal transmission involves measuring the bit error rate (BER), a critical metric that quantifies the proportion of bits received incorrectly out of the total bits sent. The BER directly measures a system's transmission accuracy and is defined as

$$\text{BER} = \frac{\text{Number of bit errors}}{\text{Total number of bits transmitted}}. \tag{11}$$

This parameter is the essential metric for evaluating transmission quality and for comparing different techniques and methods.

Another useful simplified metric, error vector magnitude (EVM), is often used as a measure of the quality of transmission and system performance. It compares the ideal symbol points (e.g., points in the complex plane as illustrated in Figure 1) to the actual symbol points received, providing insight into the distortion induced during transmission (here summation is over all symbol points):

$$\text{EVM} = \sqrt{\frac{\sum (\text{Ideal symbol point} - \text{Received symbol point})^2}{\sum (\text{Ideal symbol point})^2}}. \tag{12}$$

In the subsequent sections, we discuss the methodology of applying NFT in optical communications.

3 | Methodology of Application of NFT in Communications

Data are sent as a sequence of symbols that include some overheads. In many conventional optical communication systems, particularly those used in long-haul and high-capacity networks, these packets are typically rather long. Therefore, one can treat information flows as (effectively) continuous [52, 53]. Data in such systems are constantly transferred through the channel with some small overheads allocated for clock recovery. A continuous signal imposes certain limits on the applicability of the NFT. Currently, the most efficient and best developed numerical NFT methods are for vanishing boundary conditions. Therefore, for application of these techniques, signals must be transmitted in packets with sequences of zero symbols in between, that is called "burst" mode transmission.

To apply IST/NFT methods for potentials with vanishing boundary conditions, in this work, we consider the so-called burst-mode transmission, as schematically shown in Figure 2. Information is coded over time intervals T_b. The guard interval, T_g, is the time interval between separate bursts, "guarding" them from

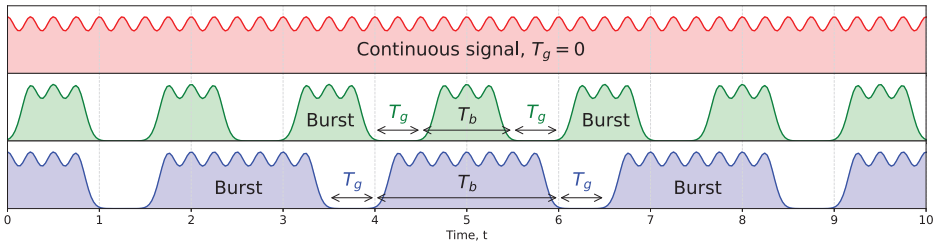

FIGURE 2 | The schematic representation depicts the burst mode with different ratios of T_g/T_b. The first row illustrates a continuous signal without a guard interval ($T_g = 0$), the second row shows a guard interval that is half the length of the burst size ($T_g = 0.5T_b$), and the third row demonstrates when the guard interval is one fourth of the burst length ($T_g = 0.25T_b$).

overlapping due to dispersive broadening of the signal. The top panel of the figure shows a schematic representation of a continuous signal. In this case, there is no time "gap" between separate bursts, so the signal is continuous and the guard interval, T_g, is zero. The second and third panels illustrate the case where T_g is not zero. Here, we have a gap between bursts.

During propagation, the signal can be substantially altered and broadened due to dispersion effects, which consequently leads to a reduction in the gap between consecutive signals. The size of this gap is directly dependent on the propagation distance and should be introduced, respectively. At low signal powers (in the linear propagation limit), this dispersive broadening can be completely reversed at the receiver, either optically or electronically. However, nonlinear interactions result in complex effects on the signal that cannot be reversed with dispersion compensation alone. Due to dispersion broadening, which can extend over several hundred symbol intervals in long-distance optical communication systems, further internal nonlinear interactions within the signal can cause one transmitted symbol to be influenced by very distinct neighbors (across hundreds of neighboring symbols). That's why the use of NFT techniques, which can mitigate both nonlinear and dispersive effects, can be beneficial compared to dispersion compensation alone [34]. NFT can integrate both dispersion and nonlinearity compensation into signal processing. Note that the compensation on both dispersion and nonlinearity can be also done by digital backpropagation (DBP) [54] using the split-step Fourier method (SSFM) [52], which iteratively computes the signal evolution in small steps over both the frequency and spatial domains. Although the DBP based on few steps per span remains an important tool, the NFT-based approaches [55] potentially can offer a trade-off between complexity of direct and inverse NFT (INFT) and just one step spatial evolution in the nonlinear spectral domain.

As mentioned above, the most efficient NFT algorithms are developed for signals with vanishing boundary conditions. This implies that we should somehow divide the signal into parts that can be processed separately. This can be achieved not with a continuous signal, but with bursts of a particular duration separated by guard intervals. In this case, we can potentially analyze each burst independently. In an ideal scenario (a pure NLSE channel), NFT would perfectly restore the deterministic signal distortions after propagation. In general, the size of the guard interval should depend on the burst broadening. The broadening, T_d, can be estimated as follows: $T_d = \beta_2 \cdot \Omega \cdot L$, where β_2 is the group velocity dispersion parameter of the fiber, L is the propagation distance, and Ω is the signal bandwidth (in the frequency domain).

As soon as we have a sequence of bursts, each of which broadens to both sides in the time interval, the guard interval that would allow us separate processing of the bursts can be estimated as (see [5])

$$T_g = 2T_d = 2 \cdot L \cdot \beta_2 \cdot \Omega. \tag{13}$$

This estimate also approximately coincides with the estimate for the soliton scattering velocity in the considered signals. If we use the maximum value of real discrete eigenvalues $\xi_{\max}$ (gives the soliton velocity $2\xi_{\max}$), for considered signals, then we can obtain an estimate for the soliton spread in dimensional variables:

$$T_d = 2\xi_{\max} * L * (T_0/L_D).$$

Thus, the guard interval in burst-mode transmission depends on the propagation distance, which must be considered during system design. However, selecting a large enough guard interval to ensure the "independence" of each burst from others is impractical, as it results in most of the available time intervals (bandwidth) not carrying information. SE measures how effectively a communication system uses its available bandwidth to transmit data. It is defined as the data rate (in bits per second) divided by the bandwidth (in Hertz) used for data transmission. The higher the SE, the more data can be transmitted in a given amount of bandwidth, making the resource use more efficient. Adding a gap that does not bear information to the continuous signal evidently decreases the overall transmission efficiency. In general, each telecommunication format has its own SE. In our case, NFT is a common approach that does not depend on the format, so the main ideas can be applied to any system. In this context, we want to introduce the term normalized spectral efficiency (NSE), which is simply the spectral efficiency of the signal divided by the maximum format SE (in our case, when the transmission is continuous without guard intervals). NSE can be defined as follows:

$$\mathrm{NSE} = \frac{T_b}{T_b + T_g} = \left(1 + \frac{T_g}{T_b}\right)^{-1}. \tag{14}$$

In the limiting cases, $NSE = 1$ when $T_g = 0$ (fully utilizing the available spectrum), and $NSE \to 0$ as $T_g/T_b \to \infty$, indicating decreased efficiency as the guard interval increases.

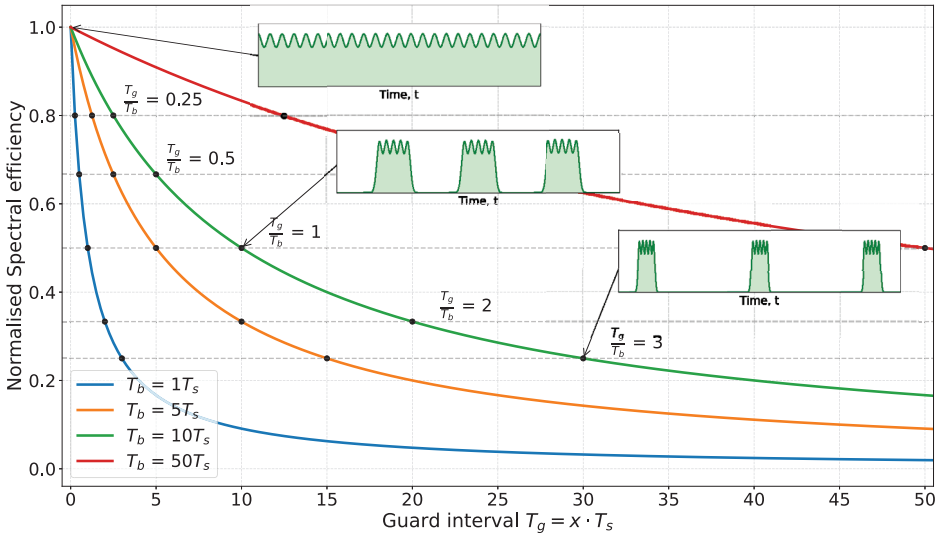

FIGURE 3 | The dependency of normalized spectral efficiency on the guard interval T_g size for burst mode transmission. Different lines indicate changes in efficiency for varying burst sizes: blue for $T_b = T_s$, orange for $T_b = 5T_s$, green for $T_b = 10T_s$, and red for $T_b = 50T_s$. The right part of the figure provides a schematic of different T_g/T_b ratios: the first for a continuous signal without a guard interval, the second for a guard interval equal to the burst length, and the third for a guard interval equal to the three burst lengths.

Figure 3 illustrates the relationship between NSE and the length of the guard interval T_g for different burst sizes (both guard interval and burst size T_b are defined in terms of the symbol interval T_s, $T_b = N \cdot T_s$). The figure shows that increasing the burst size slows the decrease in SE. This suggests that creating and analyzing very long bursts can enhance the overall SE of a system.

We summarize the methodology for applying NFT for signal processing at the receiver as follows:

1. Receive the signal and slice it in the middle of the guard intervals to isolate the bursts.
2. Apply NFT to restore the transmitted burst, incorporating the three steps of NFT outlined earlier.
3. Decode data from the processed bursts.

The larger the burst, the more data can be restored in a single application of NFT, improving SE. However, the processing of excessively long bursts is constrained by the capabilities of current NFT algorithms.

As the evolution of the nonlinear spectra with distance is trivial in the NFT domain, this paper mainly focuses on the NFT's ability to process individual bursts. The ultimate goal is to process as long a timing burst as possible to maximize the system's SE. Figure 4 illustrates the NFT coefficients and spectrum for bursts. The top image shows a burst of 64 symbols, and the bottom image displays a burst of 256 symbols, with the average signal power remaining constant. In both cases, the first row schematically represents the burst mode (with several bursts shown, but only one burst used for analysis). The second row in each image, for comparison, presents the conventional Fourier spectrum $\tilde{q}(\hat{\nu})$ of the burst $q(t)$ on the left, depending on the dimensionless frequency $\hat{\nu}$, the continuous nonlinear spectrum—the NFT reflection coefficient $r(\xi)$ in the middle (x-axis representing the nonlinear frequency ξ), and the discrete eigenvalues—the discrete spectrum ζ_k on the right. For both smaller and larger bursts, the significant part of the reflection coefficient $r(\xi)$ typically spans the spectral interval $[-3, 3]$. Outside of these boundaries, the amplitude decreases drastically toward zero as the absolute value of the nonlinear frequency increases. The computation of the continuous spectrum does not pose a particularly difficult problem—fast and precise numerical methods are well-developed, which we will detail in the following section. The more interesting and essential part of the nonlinear spectrum is depicted on the right pane, showing the discrete spectrum corresponding to the considered burst. It is important to note that for the discrete spectrum ζ_k, all values lie above the real axis. For some values, the imaginary part of ζ_k is relatively small (around 10^{-4}); for better visualization, the size of the dots is increased, making them appear as if intersecting the real axis, though this is not the case. By "smaller" and "bigger" sizes of the burst, we refer to its time duration or the number of symbols, which are equivalent. It is observed that a "smaller" burst with the same average power has fewer discrete eigenvalues. Conversely, the longer the burst, the greater the number of discrete eigenvalues (in this case, the fraction of energy associated with the continuous spectrum decreases, as will be shown later.). We can go deeper and make the following observation: the larger the number of discrete eigenvalues, the lower the accuracy of the NFT algorithms (see the study of the accuracy of algorithms for the direct NFT in [56] and examples of reconstruction of multisoliton solutions in [57]). This is the results of the INFT operation, which in most numerical approaches requires precise calculation of the kernel $\Sigma(z)$ (see Equation 4) and solving the GLME (5).

As mentioned in the introduction, in our case of anomalous dispersion medium, both dispersion and soliton components can be present in the signal. However, the presence of the soliton component depends on several factors, primarily related to the average signal power. In scenarios of low signal amplitude, the NFT operation converges to the conventional Fourier transform, and the reflection coefficient essentially represents the Fourier

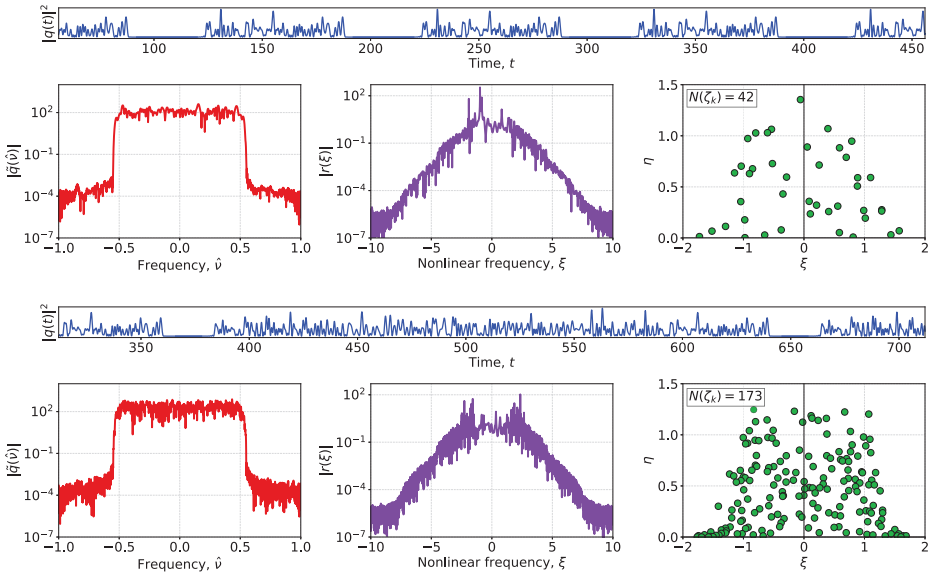

FIGURE 4 | Example of the nonlinear Fourier spectrum for bursts: the upper picture for signal with 64 symbols, the lower with 256. Each picture includes: the first row showing a schematic of burst mode, and the second row presenting the conventional Fourier spectrum $\tilde{q}(f)$ depending on the dimensionless frequency $\hat{\nu}$ on the left, the nonlinear reflection coefficient $r(\xi)$ (continuous nonlinear spectrum) in the middle, and the discrete spectrum ζ_k on the right.

image of the signal, albeit with some scaling [58]. Conversely, as the signal power increases, the divergence between the conventional Fourier and nonlinear Fourier transform becomes more pronounced. The precise conditions under which discrete eigenvalues (soliton components) appear in smooth signals can be determined analytically. For a simple rectangular impulse, this threshold can be explicitly calculated [59]. For more complex systems, where the theoretical computation of soliton presence is not feasible, several studies have explored the conditions under which a soliton becomes part of the signal [60, 61]. In addition, more innovative approaches, such as the use of neural networks to compute the number of discrete states, are being investigated [62].

4 | Key NFT Numerical Algorithms

In this section, we provide a concise overview of the key numerical methods used in both direct and inverse NFT without delving into technical details.

Direct NFT involves decomposing a signal into its nonlinear spectral components: the continuous spectrum, which represents the radiation or background modes, and the discrete spectrum, which is associated with solitonic components. The calculation of the continuous spectrum typically involves solving the ZSP, a pair of coupled ordinary differential equations (ODEs). There are various algorithms available for solving ODE systems, tailored to the specific properties of the Zakharov–Shabat system such as system stiffness and the preservation of the system's invariants. The following methods utilize transfer matrices, where the solution is obtained by repeatedly multiplying the initial data by matrices:

- Ablowitz–Ladick method with normalization of the transfer matrix (second order of approximation) [56];
- exponential methods: the Boffetta–Osborne method (second order) [63], ES4 and ES6 schemes of fourth and sixth orders, respectively, which use Magnus expansion, as well as variants of these schemes, in which the matrix exponential is calculated using the Padé series expansion [64];
- commutator-free quasi-Magnus schemes (CFQM) [65, 66], also using Magnus decomposition, but on a nonuniform grid;
- three-exponential scheme TES4 [67] of the fourth order, as well as its variants that differ in the method of splitting the central exponential [68];
- scheme CT4 (conservative transformed) of fourth order [69].

Most of the considered algorithms allow the so-called "fast" calculation (fast NFT—FNFT). The name of the approach is due to the reduction in the number of arithmetic operations for calculating the continuous spectrum from $O(M^2)$ to $O(M \log_2^2 M)$ [70, 71]. The reduction in the number of operations here is achieved by fast computing the product of transfer matrices technique and fast multiplication of polynomials using fast Fourier transform (FFT) [71–73]. Instead of multiplying the vector of initial data by the transfer matrix for each time step, all polynomial transfer matrices are first multiplied, which gives the complete transfer matrix $T(\xi)$ as a polynomial in ξ.

The discrete spectrum is characterized by eigenvalues and corresponding norming constants. To find the eigenvalues, it is necessary to find the zeros ζ_k of the function $a(\zeta)$ in the upper half-plane. Most existing approaches can be divided into three main categories:

- iterative methods for finding the roots of a complex equation $a(\zeta_k) = 0$ [56]: Newton's method, secant method, and Muller's method;

- methods using some partition of the complex plane or movement along it along trajectories: method of contour integrals [74, 75], phase jump tracking (PJT) method [76, 77], and adaptive algorithm based on trust regions [78];
- solution of the eigenvalue problem for a certain matrix: method based on constructing a certain polynomial and finding its roots by finding the eigenvalues of the corresponding accompanying matrix using QR/QZ decomposition, finite difference method [79], Ablowitz–Ladick scheme for solving a discrete spectral problem [79], Fourier collocation method [79–81], and algorithm based on the Graffe–Lobachevsky transform [73].

There are also hybrid methods: any combination of the approaches described above. For example, solutions obtained by eigenvalue search methods can be used as initial guesses for starting iterative search methods.

Calculating norming constants is a challenging task due to the presence of rapidly growing components and high sensitivity to initial data [82–84]. Many approaches have been proposed to improve the accuracy of calculating these quantities. In particular, when calculating normalization constants for eigenvalues whose imaginary part is greater than one, stability problems arise. In such cases, a bidirectional method is used, based on solving the ZS system with left and right initial data [83–85].

INFT reconstructs the time-domain signal from its spectral components. This process is inherently more complex than the direct transform due to the need to accurately synthesize both continuous and discrete spectral contributions. Several approaches to signal reconstruction from a nonlinear spectrum are presented in the literature:

- solving the Riemann–Hilbert problem [86];
- methods based on integrating the GLME: a method transitioning to a system of equations in partial derivatives [87], the Toeplitz inner bordering (TIB) method [88, 89] and its block version—generalized TIB (GTIB) [57], and high-order GTIB [90, 91], the integral layer-by-layer recovery algorithm [92, 93], and the algorithm for parameterizing the kernels of the GLME by polynomials [94]. Fast schemes are also proposed [95–97] involving fast layer-peeling algorithm and fast Darboux transform (FDT).

In [98], it is shown that methods based on the numerical solution of the GLME are more accurate compared to those based on factorization for solving the Riemann–Hilbert problem. In the case of a pure continuous spectrum, time-reversed forward NFT algorithms can be utilized to implement INFT [41, 98], positioning the INFT as a counterpart to the direct NFT, akin to the general Fourier transform. For a purely discrete spectrum, the most effective method is the Darboux transform (dressing method) [84]. The Darboux method is also applicable in scenarios involving a combination of continuous and discrete spectra [99] but requires preliminary inversion of the continuous spectrum (e.g., using GTIB [90, 91]).

5 | Results

One of the objectives of this work is to discuss the boundaries and limitations of using NFT methods for reconstructing conventional telecommunication signals transmitted in burst mode. Processing long bursts with NFT presents significant challenges. A primary challenge is the accurate computation of a large number (up to several thousands) of discrete eigenvalues and subsequent reconstruction of such a complex signal. The speed of these calculations is also crucial for the potential practical implementation of NFT techniques in the future. Initial experiments have demonstrated that in some cases omitting even a small number of discrete eigenvalues can significantly impact the accuracy of signal reconstruction.

An intriguing computation approach recently developed is the so-called PJT with an adaptive step [76, 77]. This method achieves both high accuracy in determining large discrete spectra and rapid processing. It utilizes an efficient sixth-order exponential scheme (ES6) with a ninth-order Padé approximation for the matrix exponential. Nevertheless, even with this advanced approach, searching for discrete eigenvalues remains the most time-consuming step in the process. Norming constants were evaluated using bidirectional approach [83, 85].

We should note here that the need to use high-order methods is determined by the specifics of the problem: the signal is determined on a very coarse grid—only two samples per symbol are used. Under such conditions, the only way to reduce the computational error of the form Ch^p, $C = \text{const}$, which depends on the step h along the computational grid, is to use high-order methods with large p. This is especially noticeable when calculating a discrete spectrum. Using second-order methods, for example, Ablowitz–Ladik's scheme, it is difficult to calculate a discrete spectrum on such a computational grid correctly. However, we must also acknowledge the lack of developed high-order fast algorithms for the inverse problem.

For the INFT of the continuous spectrum, we used the fast layer-peeling method from the FNFT library [100], known as the Ablowitz–Ladik scheme. This method is efficient when the number of computational nodes is a power of two. Consequently, we adjusted the length of the computational domain (in symbols) to the nearest power of two. To enhance the stability of the inverse transform and improve the accuracy of phase jump detection on the real axis, we increased the sampling rate of the continuous spectrum by up to a factor of 16.

The contributions from the discrete spectrum were integrated separately using the Darboux method from the FNFT library. It was noted that in the case of high nonlinearity, problems with signal recovery arise due to the Darboux method. One of the reasons is that when adding the contribution of the next soliton to the signal, we get a division of two large values close to the double precision limit. There are cases in the calculations when the signal cannot be calculated at all. In this paper, we propose a new approach to recovering signals with high nonlinearity and a large number of discrete eigenvalues. First, it is necessary to presort the discrete eigenvalues in descending order of the imaginary part value (this step is already implemented in the FNFT library).

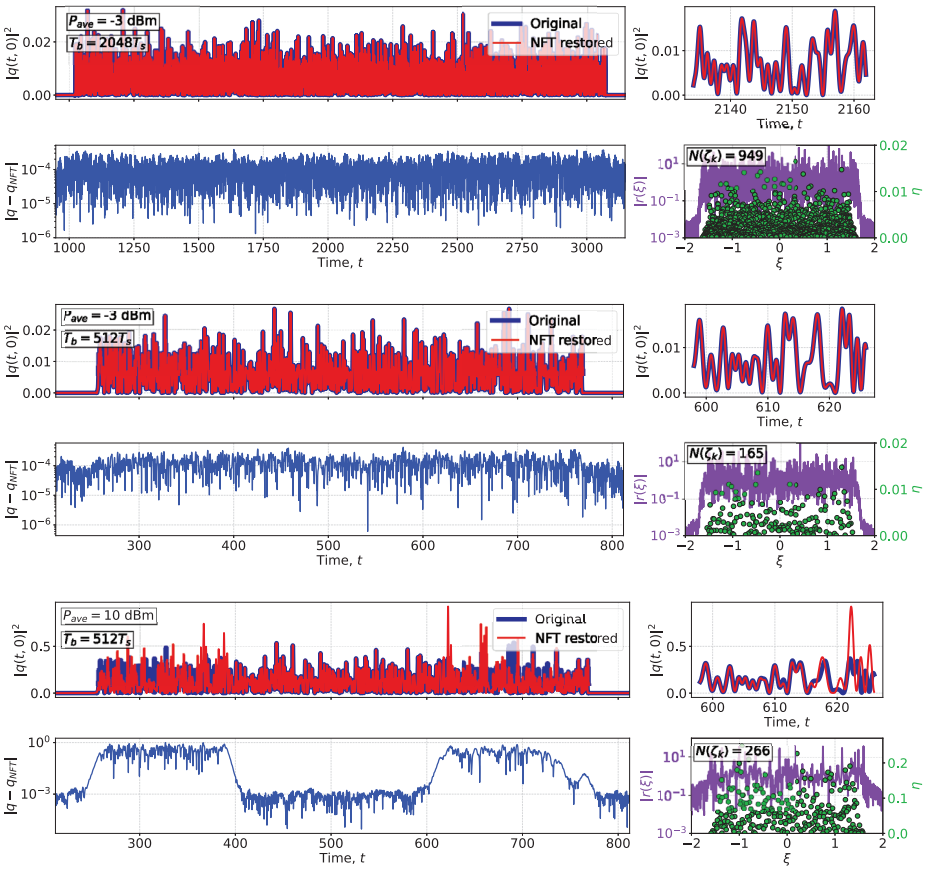

FIGURE 5 | Three examples of how NFT algorithms perform back-to-back transformations are illustrated. Each example follows the same structure: In the first pane on the left, a blue line represents the original signal $q(t,0)$, while a red line depicts the result of the signal reconstruction using NFT $q_{NFT}(t,0)$. Directly below, the absolute error $|q(t,0) - q_{NFT}(t,0)|$ is displayed. On the right column, a zoomed section of the signal from the left pane is shown for detailed examination, with the associated NF spectrum presented below it. Here, green dots indicate the discrete spectrum ζ_k, and a purple line shows the amplitude of the nonlinear coefficient $|r(\xi)|$.

Then, at a certain step, when adding another discrete eigenvalue disrupts the calculation or values at the double precision limit occur, the recovery procedure stops. That is, we sacrifice small discrete eigenvalues for the opportunity to correctly obtain the recovered signal. If the number of removed discrete eigenvalues is small, in most cases this procedure allows maintaining the BER value at the same level. We stopped the calculation at the moment when NaN ("not a number") first appeared in the loop. This happens when dividing by zero when calculating an expression

$$\beta = \frac{\phi_1 - b(\zeta_k)\psi_1}{\phi_2 - b(\zeta_k)\psi_2},$$

where $\psi_{1,2}$ and $\phi_{1,2}$ are the components of the Jost solutions used in one step of the Darboux method. To do this, it is enough to check the next obtained value of $q(t)$ for NaN or to check equality to zero in the denominator in the expression for β.

Figure 5 presents examples of back-to-back transformation (without propagation): forward NFT to calculate the NF spectrum and scattering coefficients, and INFT to restore the original signal from scattering data within the framework of the general approach to signal reconstruction by the Darboux method with preservation of all discrete eigenvalues. The figure shows three examples: the first pane on the left displays a blue line corresponding to the original signal $q(t,0)$, while the red line illustrates the result of NFT-based signal reconstruction $q_{NFT}(t,0)$. Below the first pane, the absolute error $|q(t,0) - q_{NFT}(t,0)|$ is depicted. On the right column, a zoomed section of the signal example from the left is shown. Below in the right column, the associated NF spectrum is presented: green dots represent the discrete spectrum ζ_k, and the purple line indicates the amplitude of the nonlinear coefficient $|r(\xi)|$. All three parts of the figure follow this structure.

The upper part of Figure 5 illustrates a burst with 2048 symbols ($T_b = 2048T_s$) at an average signal power of −3 dBm. Throughout the full time interval, the error remains at an average level of 10^{-4}, demonstrating good NFT restoration accuracy. In the lower right pane, it is noted that this burst contains 949 discrete eigenvalues in its NF spectrum, with the amplitude (imaginary part) consistently at 0.01. The central part of Figure 5 displays a burst with 512 symbols ($T_b = 512T_s$) at the same average power level of −3 dBm. The NFT restoration accuracy mirrors that of the larger 2048-symbol burst, with the absolute error predominantly around the 10^{-4} level. As anticipated, the smaller burst features fewer discrete eigenvalues—165 in this case—consistent with the expectation that larger bursts will contain more solitons (as represented by discrete NF spectrum) at the same average power level (see [61] for details).

A more complex and challenging scenario in which the problems of Darboux method are revealed is depicted in the lower part of Figure 5, where a burst of 512 symbols ($T_b = 512T_s$) is presented at a higher average signal power of 10 dBm. The discrete spectrum, shown in the lower right pane, includes 266 eigenvalues, nearly a hundred more than the similar-sized burst at −3 dBm. Notably, the maximum value of the imaginary part of discrete eigenvalues reaches approximately 0.2, which is 20 times greater than in lower power scenarios. This substantial increase in the imaginary part values could potentially lead to higher inaccuracies in numerical calculations, given that they influence the $e^{-i\zeta_k t}$ factor in the kernel $\Sigma(z,t)$ used in GLME (5) (see [57]). In Figure 5, the left column demonstrates how NFT reconstructs the original signal. Notably, in the central region, specifically between 400 and 600 dimensionless time units, the restoration quality is adequately high and stable, with an absolute error maintained at the level of 10^{-3}. However, outside this interval, the restoration accuracy significantly deteriorates, leading to entirely erroneous results where the absolute error reaches the level of the signal amplitude itself. The zoomed view in the right upper pane highlights specific issues with accuracy. In the time interval $t \in [610, 620]$, discrepancies between the restored and the original signals begin to emerge, and post $t = 620$, the restored signal becomes completely inaccurate. A similar degradation in signal reconstruction is observed at the opposite end of the time scale, where the value of t drops below −400.

As mentioned previously, a significant factor contributing to numerical inaccuracies in NFT is the term $e^{-i\zeta_k t}$, where $-i\zeta_k t = -i(\xi_k + i\eta_k)\cdot t = (-i\xi_k + \eta_k)\cdot t$. The larger values of the imaginary part of the discrete spectrum, when multiplied by time, result in a larger exponential factor that exceeds the accuracy limits of standard floating-point numbers. This is one of the critical limitations of NFT algorithms, particularly evident when attempting to increase the average power beyond a certain threshold. Such limitations lead to increased EVM and BER, highlighting the numerical challenges. Moreover, while numerical inaccuracies are one aspect, the complete failure of INFT restoration presents an even more significant challenge. This issue is a primary constraint that restricts further increases in burst size within the framework of the general approach to signal reconstruction by the Darboux method with preservation of all discrete eigenvalues.

Utilizing NFT with vanishing boundary conditions, we are presently constrained to burst-mode transmission. In such scenarios, we aim to employ the longest possible time bursts to maintain SE (as indicated in Equation (14) and Figure 3). However, longer bursts necessitate managing a greater number of discrete eigenvalues (as illustrated in Figure 5) and the precise calculation of their spectral coefficients r_k. In addition, there is a need for accurate methods for INFT capable of handling such a large quantity of discrete eigenvalues. These requirements define the upper limits on the burst size that can be effectively processed, which will be discussed further.

In this section, we analyze the statistics of 1000 bursts at an average signal power of −3 dBm, with burst sizes ranging from 200 symbols ($T_b = 200T_s$) to 4000 symbols. For each burst size, we measured the average EVM and calculated the resulting BER. Figure 6 demonstrates how BER (black dots) and EVM (blue line with markers) vary with the number of symbols in the burst N_{symb} for the general Darboux method and modified. Initially, from 200 to approximately 2500 symbols, the BER remains at zero, indicated by the green zone. This zero BER suggests perfect signal restoration across all 1000 bursts, despite a gradual increase in EVM with burst size, indicating that numerical errors remain below the threshold for error onset. The threshold is breached at 2500–2600 symbols, where a slight rise in average EVM corresponds to the emergence of a nonzero BER. Although this initial change is not drastic—remaining below the FEC level of $4 \cdot 10^{-2}$—this change signals a warning (yellow region), suggesting that while error rates are low, additional techniques are required to maintain near-errorless information transmission (BER after FEC becomes below 10^{-15} [101]). The graph reveals a consistent increase in EVM with burst size, logically reflecting the rising challenge of accurately handling an increasing number of discrete eigenvalues. It is noteworthy that after 3300 symbols both EVM and BER increase sharply, but BER never exceeds the FEC threshold for the considered burst lengths for modified Darboux method. The general approach gives sharp escalation of EVM and BER, and by 3400 symbols, the BER exceeds the FEC threshold.

The left part of Figure 7 addresses INFT failures for the general approach to signal reconstruction by the Darboux method—the frequency of INFT errors relative to the total number of bursts per parameter set, illustrating the reliability of INFT with preservation of all discrete eigenvalues. Beyond 2500 symbols, INFT algorithms fail rate increases, resulting incomplete information loss from bursts and a corresponding rise in average BER. A significant jump in EVM between 3300 and 3400 symbols highlights the point where numerical algorithms begin to fail (return an error). Thus, post-3300 symbols, the zone is marked in red, indicating regions where NFT algorithms fail to reliably restore the signal.

What causes the INFT to fail? A simple explanation can be obtained from Figure 7 (right). Here, the red line represents the portion of the total signal energy (see Equation 6) attributed to the discrete spectrum—namely, solitons. The blue line chart is the average total number of discrete eigenvalues in the data set for each number of symbols. The zones are color-coded similarly to Figure 6—green for zero BER, yellow for BER below the FEC threshold, and red for BER exceeding 4×10^{-2}. Initially, we observe that as the number of symbols increases, the proportion of energy corresponding to the discrete spectrum quickly rises and stabilizes at the end of the green zone—around 2000 symbols. Concurrently, the count of discrete eigenvalues nearly linearly increases with the burst size. This trend aligns with the general understanding that longer signals in the time domain typically contain more solitons. Given that the average signal power remains constant, the increase in total number of symbols in a burst leads to a greater allocation of the total energy to solitons rather than to the dispersive part of the signal. Hence, the number of solitons increases while their average imaginary part stays consistent. This scenario creates numerical challenges for NFT methods: the factor $e^{-i\zeta_k t}$ becomes numerically unstable, leading to INFT failures. Consequently, once the number of discrete eigenvalues reaches a certain threshold—in this case, around 2600 for −3 dBm—current numerical methods struggle to deliver reliable results, manifesting in the observed INFT failures. Note that problems also arise in the case of normal dispersion, when

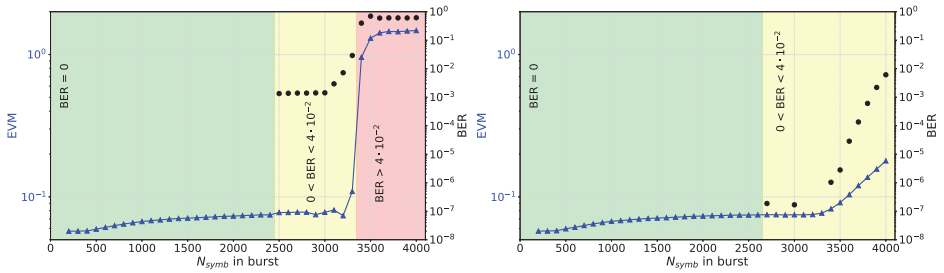

FIGURE 6 | The left plot displays the BER (black dots, values on the left axis) and EVM (blue line, values on the right axis) depending on the number of symbols in each burst when the Darboux method uses all discrete eigenvalues. The right plot displays BER and EVM when the Darboux method uses only those discrete eigenvalues whose addition does not lead to calculation failure. All data points represent the average values from the statistics of 1000 different burst samples, with an average signal power of −3 dBm. The plots are divided into regions: the green region indicates a BER of 0, where all symbols are correctly decoded; the yellow region indicates a BER less than $4 \cdot 10^{-2}$, suitable for hard decoding with forward error correction (FEC); and the red region where the BER exceeds the FEC threshold.

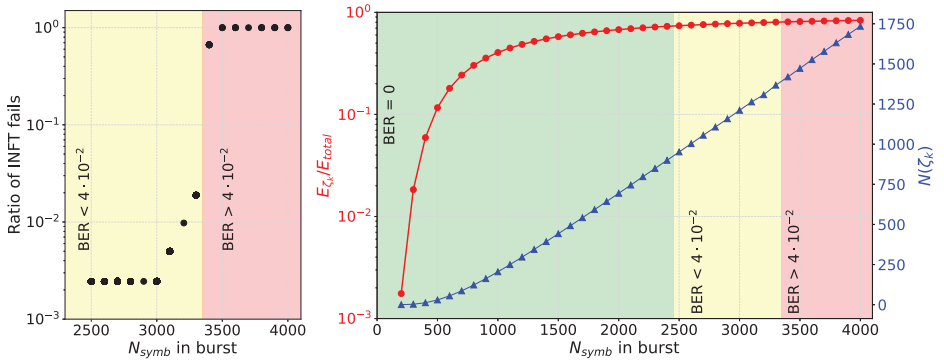

FIGURE 7 | The left plot illustrates the proportion of instances where the inverse NFT (INFT) completely failed, returning an entirely incorrect result when the Darboux method uses all discrete eigenvalues. The red line on the right plot represents the ratio of energy associated with the discrete spectrum (ζ_d) to the total signal energy as a function of the number of symbols in the burst. The blue line indicates the average number of discrete eigenvalues in the nonlinear Fourier spectrum relative to the burst size. The plots employ the same color coding as in Figure 6: the green region signifies a BER of 0, indicating all symbols are correctly decoded; the yellow region indicates a BER less than $4 \cdot 10^{-2}$, suitable for hard decoding at the forward-error-correction (FEC) level; and the red region where the BER exceeds this FEC threshold. All data points are derived from the average values of 1000 different burst samples.

there is no discrete spectrum. One possible solution here is to use high-order methods for INFT [90, 91].

Up until now, we considered the broad context of using the NFT approach for telecommunication signal processing. In this section, we show examples of the performance analysis for single-channel 16-QAM WDM signal transmission over 12 spans of 80 km standard single-mode fiber (SSMF), resulting in a total distance of 960 km. The average signal power remains the same at −3 dBm. The main propagation model used is the path-averaged NLSE (2). To focus on the nonlinear transmission impairments, we also assume no additional noise. All parameters of the fiber-optic communication line under consideration are presented in Table 1.

Figure 8 presents the same plot as Figure 6 but for signal restoration using the complete three-step NFT approach: forward NFT, compensation of scattering data evolution according to the propagation distance, and INFT. The black dots show the resulting BER after full signal processing, and the blue line shows the corresponding EVM for each number of symbols in one burst N_{symb}. The color scheme remains the same: green, yellow, and red zones indicate zero, less, and more than FEC level BER, respectively. For the modified Darboux method, there are no significant difference in the borders of the colored regions between the cases without propagation (Figure 6) and with propagation.

For the general Darboux method, the NFT approach begins to show insufficiently accurate results after 3100 symbols in a burst (compared to 3300 for the case without propagation). In addition, the yellow region starts at a much lower number of symbols—right after 1000, while it was 2400 for the back-to-back system. This is not surprising—when we add propagation, we include the second NFT step into account, which adds additional inaccuracy into the final calculation. As shown before, for each discrete eigenvalue in the NF spectrum, we must calculate scattering coefficients and then multiply them by a phase factor $e^{-2i\zeta_k^2 z}$ that contains a real-value exponent that depends on the real and imaginary part of the eigenvalue. This phase factor is defined by the propagation distance, so the overall value of the exponent highly depends on the accuracy of the eigenvalue calculation. As numerical calculations do not guarantee total convergence, sometimes numerical errors and instability can occur, leading to errors in signal reconstruction. Therefore, we

TABLE 1 | Channel and signal parameters.

Parameter	Symbol	Value	Parameter	Value
Span length	L_{sp}	80 km	Central wavelength	1.55 μm
Number of spans	N_{sp}	12	Average signal power	−3 dBm
Attenuation	α	0.2 dB/km	Modulation format	16-QAM
Group-velocity dispersion	β_2	−21.7 ps^2/km	Channel baud rate	67.4 GHz
Nonlinearity	γ	1.2 1/W/km	Pulse shaping	RRC with a roll-off factor of 0.1

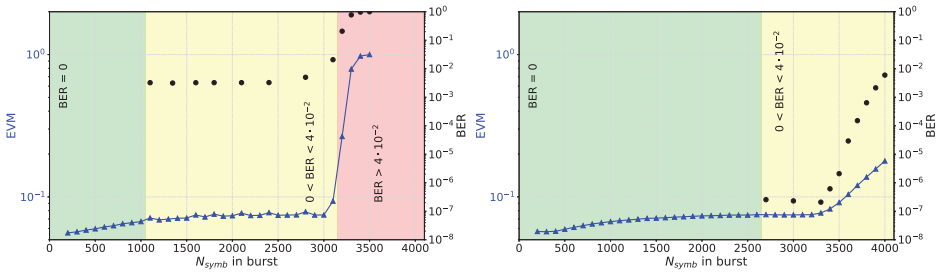

FIGURE 8 | Results for single-channel 16-QAM WDM signal propagation over 12 spans of 80 km (960 km) standard single-mode fiber (SSMF). The left plot displays the BER (black dots, values on the left axis) and EVM (blue line, values on the right axis) depending on the number of symbols in each burst when the Darboux method uses all discrete eigenvalues. The right plot displays BER and EVM when the Darboux method uses only those discrete eigenvalues whose addition does not lead to calculation failure. All data points represent the average values from the statistics of 1000 different burst samples, with an average signal power of −3 dBm. The color scheme remains the same: green, yellow, and red zones indicate zero, less, and more than FEC level ($4 \cdot 10^{-2}$) BER, respectively. The right plot illustrates the proportion of instances where the inverse NFT (INFT) completely failed, returning an entirely incorrect result.

see the consequence—with an increase in the number of symbols in a burst, we increase errors (which include dependence on propagation). The proof for this is seen on the right graph, where cases of INFT fails occur for a much "wider" region than in the back-to-back case.

Another important issue the dependence of the NFT processing performance on average signal power. As shown in the examples in Figure 5, the algorithm's performance depends on the power, and one can observe worse performance for higher power compared to low signal powers. This is logical in our noiseless model scenario—as the power decreases, we transition from a nonlinear model to a more linear one, which in the limit of very small average signal powers converges to a fully linear model that can be solved using the general Fourier transform approach (compensate dispersion in Equation (2) while the nonlinear term is zero).

To illustrate the NFT limits depending on the average signal power, we fix the burst size and vary the average power to observe the NFT performance. We choose a burst size of 512 symbols, which has good performance for back-to-back and propagation cases, allowing us to see the performance across all ranges from good cases to "complete" failures of NFT algorithms. We change the average signal power from −5 dBm up to 15 dBm and perform the same analysis as above for the 16-QAM WDM signal propagation over 12 spans of 80 km of SSMF. The results are shown in Figure 9, where each point corresponds to the statistics of 1000 data points. The colored regions represent the same logic as before. Both versions of the Darboux method behave qualitatively the same, but the modified method shows better results at an average power of up to 10 dBm. From −5 to 3 dBm, the BER remains at the zero level, indicating that the NFT perfectly restores all the signals. However, the overall accuracy represented by the average EVM increases with the power increase, and we inevitably reach the limit case where we start to receive errors (at 4 dBm level). From 4 to 6 dBm, the BER and EVM values remain at almost the same level, indicating that in this region the NFT algorithms show stable performance that does not highly depend on the average signal power. Therefore, within this region, we can change the average power (depending on practical system requirements) and maintain the same performance level. With further increases in power, at 11 dBm, the performance falls below the FEC level and decreases, as the EVM follows this tendency, as expected.

In summary, the NFT performance is affected by several factors. The first factor is the burst size—the larger the burst, the more discrete eigenvalues and corresponding scattering data need to be processed. The second factor is the average power—in the limiting case of small powers, we will have zero or very few solitons. In contrast, for high powers, we expect more discrete eigenvalues with larger imaginary parts. These two variables—the size of the burst and the average signal power—determine the size and properties of the nonlinear spectral data. Propagation distance does not affect the nonlinear spectrum, however, it changes the scattering data used in the INFT algorithm. Since distance impacts the phase factor, larger values create more numerical inaccuracies that cannot be correctly handled, affecting the overall NFT accuracy. Thus, in summary the main

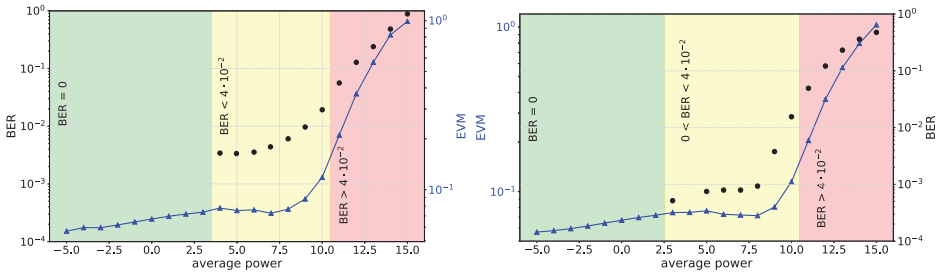

FIGURE 9 | Results for signal propagation over 960 km for different average power with fixed burst size ($T_b = 512T_s$). The left plot displays the BER (black dots, values on the left axis) and EVM (blue line, values on the right axis) depending on the number of symbols in each burst when the Darboux method uses all discrete eigenvalues. The right plot displays BER and EVM when the Darboux method uses only those discrete eigenvalues whose addition does not lead to calculation failure. All data points represent the average values from the statistics of 1000 different burst samples for each average signal power. The color scheme remains the same: green, yellow, and red zones indicate zero, less, and more than FEC level ($4 \cdot 10^{-2}$) BER, respectively. The right plot illustrates the proportion of instances where the inverse NFT (INFT) completely failed, returning an entirely incorrect result.

limiting factors of the NFT approach are: burst size, average signal power, and propagation distance. For each set of parameters, the performance can be either acceptable or not, and it needs to be checked for the particular requirements of the system.

6 | Conclusion

In this methodological paper, we discussed several important aspects and limits of the applications of IST/NFT techniques in telecommunications. The conventional Fourier transform was initially developed to solve a particular linear equation by transforming the studied function into the frequency domain, where the evolution of each spectral component is trivial. This decomposition of a function of time into frequency harmonics is nowadays also widely used for analysis and characterization of signals, without relation to any evolution. Arguably, the conventional Fourier transform became a widely used technology after the development and easy availability of the FFT. As a matter of fact, the standard Fourier transform is just one of many ways to transform a function to another domain and present it as a composition of components in that domain. In this sense, IST/NFT is also just one of many possibilities to present a signal through its nonlinear spectrum. IST/NFT can be used for solving evolution in the integrable problems (in this case, evolution according to the NLSE), but it can also be used to facilitate analysis and characterization of signals, similar to the conventional Fourier transform. The key difference between standard Fourier and NFT is the availability of devices that can implement the Fourier transform and the lack of similar hardware for the NFT. However, the IST/NFT is still a relatively young technique, and there is no fundamental reason why such hardware cannot be developed in the future. We do hope that this work can stimulate interest in developing such devices in future.

We explained in this paper how IST/NFT-based signal processing can be applied to optical fiber communications systems for the analysis of conventional optical signals. We discuss various practical challenges limiting the application of the NFT algorithms with vanishing boundary conditions in the considered burst mode transmission. On the one hand, it is important to use longer bursts to increase SE; on the other hand, longer bursts are much more challenging to process due to a large number of discrete eigenvalues. Increasing the average power required to maintain a larger SNR leads to the same problem of increasing difficulties of the NFT-based signal processing. We hope that this work, showing how the remarkable mathematical concept of IST is developing toward engineering application, will stimulate the mathematical community to look at the specific challenges of practical implementation and the engineering community to learn about opportunities offered by IST/NFT in nonlinear engineering systems.

Acknowledgments

The work of I.C. and M.P.F. were supported by the Russian Science Foundation (project no. 20-11-20040, https://rscf.ru/project/20-11-20040/). The work of E.S. and S.K.T. was supported by the EPSRC project TRANSNET.

Data Availability Statement

The data that support the findings of this study are available from the corresponding author upon reasonable request.

References

1. A. Scott, *Nonlinear Science: Emergence and Dynamics of Coherent Structures* (Oxford: Oxford University Press, 2003).

2. V. E. Zakharov, "Stability of Periodic Waves of Finite Amplitude on the Surface of a Deep Fluid," *Journal of Applied Mechanics and Technical Physics* 9 (1968): 190–194.

3. D. H. Peregrine, "Water Waves, Nonlinear Schrödinger Equations and Their Solutions," *ANZIAM Journal* 25 (1983): 16–43.

4. V. E. Zakharov and A. B. Shabat, "Exact Theory of Two-Dimensional Self-Focusing and One-Dimensional Self-Modulation of Waves in Nonlinear Media," *Soviet Physics JETP* 34 (1972): 62–69.

5. G. P. Agrawal, *Nonlinear Fiber Optics*, 5th ed. (Boston: Academic Press, 2013).

6. A. Hasegawa and Y. Kodama, *Solitons in Optical Communications* (Oxford: Oxford University Press, 1995).

7. E. Iannone, F. Matera, A. Mecozzi, and M. Settembre, *Nonlinear Optical Communication Networks* (Hoboken, New Jersey: Wiley, 1998).

8. L. F. Mollenauer and J. P. Gordon, *Solitons in Optical Fibers: Fundamentals and Applications* (Amsterdam: Elsevier, 2006).

9. E. Kuznetsov, "Solitons in a Parametrically Unstable Plasma," *Soviet Physics-Doklady* 22 (1977): 507–508.

10. A. C. Newell, *Solitons in Mathematics and Physics*, CBMS-NSF Regional Conference Series in Applied Mathematics (Society for Industrial and Applied Mathematics, 1985).

11. L. Stenflo and M. Marklund, "Rogue Waves in the Atmosphere," *Journal of Plasma Physics* 76 (2010): 293–295.

12. A. Scott, "Davydov's Soliton," *Physics Reports* 217 (1992): 1–67.

13. L. P. Pitaevskii and S. Stringari, *Bose-Einstein Condensation*, International Series of Monographs on Physics (Oxford: Clarendon Press, 2003).

14. G. Falkovich, *Fluid Mechanics* (Cambridge: Cambridge University Press, 2018).

15. M. Dunajski, *Solitons, Instantons, and Twistors*, Oxford Graduate Texts in Mathematics (Oxford: Oxford University Press, 2010).

16. J. D. Ania-Castañón, T. J. Ellingham, R. Ibbotson, X. Chen, L. Zhang, and S. K. Turitsyn, "Ultralong Raman Fibre Lasers as Virtually Lossless Optical Media," *Physical Review Letters* 96 (2006):023902.

17. S. T. Le, J. E. Prilepsky, and S. K. Turitsyn, "Nonlinear Inverse Synthesis Technique for Optical Links With Lumped Amplification," *Optics Express* 23 (2015): 8317–8328.

18. S. K. Turitsyn, J. E. Prilepsky, S. T. Le, et al., "Nonlinear Fourier Transform for Optical Data Processing and Transmission: Advances and Perspectives," *Optica* 4 (2017): 307–322.

19. J. D. Ania-Castañón, V. Karalekas, P. Harper, and S. K. Turitsyn, "Simultaneous Spatial and Spectral Transparency in Ultralong Fiber Lasers," *Physical Review Letters* 101 (2008):123903.

20. K. Tajima, "Compensation of Soliton Broadening in Nonlinear Optical Fibers With Loss," *Optics Letters* 12 (1987): 54–56.

21. M. J. Ablowitz, D. J. Kaup, A. C. Newell, and H. Segur, "The Inverse Scattering Transform-Fourier Analysis for Nonlinear Problems," *Studies in Applied Mathematics* 53 (1974): 249–315.

22. M. J. Ablowitz and H. Segur, *Solitons and the Inverse Scattering Transform* (Philadelphia: Society for Industrial and Applied Mathematics, 1981).

23. M. I. Yousefi and F. R. Kschischang, "Information Transmission Using the Nonlinear Fourier Transform, Part I: Mathematical Tools," *IEEE Transactions on Information Theory* 60 (2014): 4312–4328.

24. A. Hasegawa and T. Nyu, "Eigenvalue Communication," *Journal of Lightwave Technology* 11 (1993): 395–399.

25. R.-J. Essiambre, G. Kramer, P. J. Winzer, G. J. Foschini, and B. Goebel, "Capacity Limits of Optical Fiber Networks," *Journal of Lightwave Technology* 28 (2010): 662–701.

26. S. K. Turitsyn, J. D. Ania-Castañón, S. A. Babin, et al., "270-km Ultralong Raman Fiber Laser," *Physical Review Letters* 103 (2009): 133901.

27. I. S. Chekhovskoy, O. V. Shtyrina, M. P. Fedoruk, S. B. Medvedev, and S. K. Turitsyn, "Nonlinear Fourier Transform for Analysis of Coherent Structures in Dissipative Systems," *Physical Review Letters* 122 (2019):153901.

28. S. Sugavanam, M. K. Kopae, J. Peng, J. E. Prilepsky, and S. K. Turitsyn, "Analysis of Laser Radiation Using the Nonlinear Fourier Transform," *Nature Communications* 10 (2019): 5663.

29. S. Randoux, P. Suret, A. Chabchoub, B. Kibler, and G. El, "Nonlinear Spectral Analysis of Peregrine Solitons Observed in Optics and in Hydrodynamic Experiments," *Physical Review E* 98 (2018):022219.

30. S. K. Turitsyn, I. S. Chekhovskoy, and I. S. Fedorukw, "Nonlinear Fourier Transform for Analysis of Optical Spectral Combs," *Physical Review E* 103 (2021):L020202.

31. P. Koster and S. Wahls, "Fast and Reliable Detection of Significant Solitons in Signals With Large Time-Bandwidth Products," *Journal of Lightwave Technology* 41 (2023): 6586–6598.

32. Y.-C. Lee, M. Brühl, D.-J. Doong, and S. Wahls, "Nonlinear Fourier Classification of 663 Rogue Waves Measured in the Philippine Sea," preprint, Research Square (2022).

33. I. T. Lima, T. D. S. DeMenezes, V. S. Grigoryan, M. O'sullivan, and C. R. Menyuk, "Nonlinear Compensation in Optical Communications Systems With Normal Dispersion Fibers Using the Nonlinear Fourier Transform," *Journal of Lightwave Technology* 35 (2017): 5056–5068.

34. S. Wahls, S. Le, J. Prilepsky, H. V. Poor, and S. Turitsyn, "Digital Backpropagation in the Nonlinear Fourier Domain," in *2015 IEEE 16th International Workshop on Signal Processing Advances in Wireless Communications (SPAWC)* (IEEE, 2015), 445–449.

35. E. G. Turitsyna and S. K. Turitsyn, "Digital Signal Processing Based on Inverse Scattering Transform," *Optics Letters* 38 (2013): 4186–4188.

36. M. Yousefi and X. Yangzhang, "Linear and Nonlinear Frequency-Division Multiplexing," *IEEE Transactions on Information Theory* 66 (2020): 478–495.

37. J. E. Prilepsky, S. A. Derevyanko, K. J. Blow, I. Gabitov, and S. K. Turitsyn, "Nonlinear Inverse Synthesis and Eigenvalue Division Multiplexing in Optical Fiber Channels," *Physical Review Letters* 113 (2014):013901.

38. S. Le, J. E. Prilepsky, and S. K. Turitsyn, "Nonlinear Inverse Synthesis for High Spectral Efficiency Transmission in Optical Fibers," *Optics Express* 22 (2014): 26720–26741.

39. M. Yousefi and X. Yangzhang, "Linear and Nonlinear Frequency-Division Multiplexing," in *ECOC 2016: Proceedings of 42nd European Conference on Optical Communication* (VDE, 2016), 1–3.

40. X. Yangzhang, M. Yousefi, A. Alvarado, D. Lavery, and P. Bayvel, "Nonlinear Frequency-Division Multiplexing in the Focusing Regime," in *Optical Fiber Communication Conference* (Optical Society of America, 2017), Tu3D–1.

41. M. Yousefi and X. Yangzhang, "Linear and Nonlinear Frequency-Division Multiplexing," *IEEE Transactions on Information Theory* 66 (2019): 478–495.

42. Z. Dong, S. Hari, T. Gui, et al., "Nonlinear Frequency Division Multiplexed Transmissions Based on NFT," *IEEE Photonics Technology Letters* 27 (2015): 1621–1623.

43. V. Aref, H. Bulow, K. Schuh, and W. Idler, "Experimental Demonstration of Nonlinear Frequency Division Multiplexed Transmission," in *2015 European Conference on Optical Communication (ECOC)* (IEEE, 2015), 1–3.

44. H. Buelow, V. Aref, and W. Idler, "Transmission of Waveforms Determined by 7 Eigenvalues With PSK-Modulated Spectral Amplitudes," in *ECOC 2016: Proceedings of 42nd European Conference on Optical Communication* (VDE, 2016), 1–3.

45. V. Aref, S. Le, and H. Buelow, "Demonstration of Fully Nonlinear Spectrum Modulated System in the Highly Nonlinear Optical Transmission Regime," in *ECOC-Post Deadline Paper: Proceedings of 42nd European Conference on Optical Communication* (VDE, 2016), 1–3.

46. S. Wahls, "Generation of Time-Limited Signals in the Nonlinear Fourier Domain Via b-Modulation," in *2017 European Conference on Optical Communication (ECOC), no. 6* (IEEE, 2017), 1–3.

47. T. Gui, G. Zhou, C. Lu, P. T. L. Alan, and S. Wahls, "Nonlinear Frequency Division Multiplexing With b-Modulation: Shifting the Energy Barrier," *Optics Express* 26 (2018): 27978–27990.

48. A. Vasylchenkova, J. E. Prylepsky, N. B. Chichkov, and S. K. Turitsyn, "Multieigenvalue Communication Paired With b-Modulation," in *45th European Conference on Optical Communication (ECOC 2019)* (IET, 2019), 1–4.

49. G. R. Stibitz, *Binary Counter*, US Patent 2,307,868 (1943).

50. G. C. Clark Jr., and J. B. Cain, *Error-Correction Coding for Digital Communications* (Berlin: Springer Science & Business Media, 2013).

51. G. Keiser, *Optical Fiber Communications*, Vol. 2 (New York: McGraw-Hill, 2000).

52. G. P. Agrawal, *Fiber-Optic Communication Systems* (Wiley, 2012).

53. K. Kikuchi, "Fundamentals of Coherent Optical Fiber Communications," *Journal of Lightwave Technology* 34 (2015): 157–179.

54. E. Ip and J. M. Kahn, "Compensation of Dispersion and Nonlinear Impairments Using Digital Backpropagation," *Journal of Lightwave Technology* 26 (2008): 3416–3425.

55. S. Wahls, S. T. Le, J. E. Prilepsk, H. V. Poor, and S. K. Turitsyn, "Digital Backpropagation in the Nonlinear Fourier Domain," in *2015 IEEE 16th International Workshop on Signal Processing Advances in Wireless Communications (SPAWC)* (2015), 445–449.

56. A. Vasylchenkova, J. E. Prilepsky, D. Shepelsky, and A. Chattopadhyay, "Direct Nonlinear Fourier Transform Algorithms for the Computation of Solitonic Spectra in Focusing Nonlinear Schrödinger Equation," *Communications in Nonlinear Science and Numerical Simulation* 68 (2019): 347–371.

57. S. B. Medvedev, I. A. Vaseva, and M. P. Fedoruk, "Block Toeplitz Inner-Bordering Method for the Gelfand–Levitan–Marchenko Equations Associated With the Zakharov–Shabat System," *Journal of Inverse and Ill-Posed Problems* 31 (2023): 191–202.

58. J. E. Prilepsky, S. A. Derevyanko, and S. K. Turitsyn, "Nonlinear Spectral Management: Linearization of the Lossless Fiber Channel," *Optics Express* 21 (2013): 24344–24367.

59. M. Klaus and J. K. Shaw, "On the Eigenvalues of Zakharov-Shabat System," *Journal of Mathematical Analysis* 34 (2003): 759–773.

60. E. V. Sedov, A. A. Redyuk, M. P. Fedoruk, A. A. Gelash, L. L. Frumin, and S. K. Turitsyn, "Soliton Content in the Standard Optical OFDM Signal," *Optics Letters* 43 (2018): 5985–5988.

61. S. K. Turitsyn, E. V. Sedov, A. A. Redyuk, and M. P. Fedoruk, "Nonlinear Spectrum of Conventional OFDM and WDM Return-to-Zero Signals in Nonlinear Channel," *Journal of Lightwave Technology* 38 (2020): 352–358.

62. E. V. Sedov, I. S. Chekhovskoy, J. E. Prilepsky, and M. P. Fedoruk, "Application of Neural Networks to Determine the Discrete Spectrum of the Direct Zakharov–Shabat Problem," *Quantum Electronics* 50 (2020): 1105.

63. G. Boffetta and A. R. Osborne, "Computation of the Direct Scattering Transform for the Nonlinear Schroedinger Equation," *Journal of Computational Physics* 102 (1992): 252–264.

64. S. B. Medvedev, I. S. Chekhovskoy, I. A. Vaseva, and M. P. Fedoruk, "Fast Sixth-Order Algorithm Based on the Generalized Cayley Transform for the Zakharov-Shabat System Associated With Nonlinear Schrodinger Equation," *Journal of Computational Physics* 448 (2022):110764.

65. S. Blanes, F. Casas, and M. Thalhammer, "High-Order Commutator-Free Quasi-Magnus Exponential Integrators for Non-Autonomous Linear Evolution Equations," *Computer Physics Communications* 220 (2017): 243–262.

66. S. Chimmalgi, P. J. Prins, and S. Wahls, "Fast Nonlinear Fourier Transform Algorithms Using Higher Order Exponential Integrators," *IEEE Access* 7 (2019): 145161–145176.

67. S. B. Medvedev, I. A. Vaseva, I. S. Chekhovskoy, and M. P. Fedoruk, "Exponential Fourth Order Schemes for Direct Zakharov-Shabat Problem," *Optics Express* 28 (2020): 20–39.

68. S. B. Medvedev, I. A. Vaseva, D. I. Kachulin, I. S. Chekhovskoy, and M. P. Fedoruk, "Fast Nonlinear Fourier Transform Algorithms for Optical Data Processing," *Optics Letters* 49 (2024): 1884–1887.

69. S. B. Medvedev, I. A. Vaseva, I. S. Chekhovskoy, and M. P. Fedoruk, "Numerical Algorithm With Fourth-Order Accuracy for the Direct Zakharov-Shabat Problem," *Optics Letters* 44 (2019): 2264–2267.

70. S. Wahls and H. V. Poor, "Introducing the Fast Nonlinear Fourier Transform," in *International Conference on Acoustics, Speech and Signal Processing, Vancouver* (IEEE, 2013), 5780–5784.

71. S. Wahls and H. V. Poor, "Fast Numerical Nonlinear Fourier Transforms," *IEEE Transactions on Information Theory* 61 (2015): 6957–6974.

72. V. Vaibhav, "Fast Inverse Nonlinear Fourier Transformation Using Exponential One-Step Methods: Darboux Transformation," *Physical Review E* 96 (2017):063302.

73. A. L. Delitsyn, "Fast Algorithms for Solving the Inverse Scattering Problem for the Zakharov–Shabat System of Equations and Their Applications," *Mathematical Notes* 112 (2022): 198–217.

74. L. M. Delves and J. N. Lyness, "A Numerical Method for Locating the Zeros of an Analytic Function," *Mathematics of Computation* 21 (1967): 543–543.

75. A. Vasylchenkova, J. E. Prilepsky, and S. K. Turitsyn, "Contour Integrals for Numerical Computation of Discrete Eigenvalues in the Zakharov-Shabat Problem," *Optics Letters* 43 (2018): 3690–3693.

76. I. S. Chekhovskoy, S. B. Medvedev, I. A. Vaseva, E. V. Sedov, and M. P. Fedoruk, "Introducing Phase Jump Tracking—A Fast Method for Eigenvalue Evaluation of the Direct Zakharov-Shabat Problem," *Communications in Nonlinear Science and Numerical Simulation* 96 (2021):105718.

77. I. S. Chekhovskoy, S. B. Medvedev, I. A. Vaseva, E. V. Sedov, and M. P. Fedoruk, "Fast Eigenvalue Evaluation of the Direct Zakharov-Shabat Problem in Telecommunication Signals Using Adaptive Phase Jump Tracking," in *2021 Conference on Lasers and Electro-Optics Europe & European Quantum Electronics Conference (CLEO/Europe-EQEC)* (IEEE, 2021).

78. J. He, L. Jianping, Y. Qin, et al., "Adaptive Trust-Region-Based Algorithm for the Discrete Eigenvalue Evaluation of the Direct Nonlinear Fourier Transform," *Optics Letters* 47 (2022): 4195–4198.

79. M. I. Yousefi and F. R. Kschischang, "Information Transmission Using the Nonlinear Fourier Transform, Part II: Numerical Methods," *IEEE Transactions on Information Theory* 60 (2014): 4329–4345.

80. Y. Jianke, *Nonlinear Waves in Integrable and Nonintegrable Systems*, Vol. 16 (Philadelphia: Society for Industrial and Applied Mathematics, 2010).

81. F. J. García-Gómez and V. Aref, "Statistics of the Nonlinear Discrete Spectrum of a Noisy Pulse," *Journal of Lightwave Technology* 37 (2019): 3563–3570.

82. A. Gelash and R. Mullyadzhanov, "Anomalous Errors of Direct Scattering Transform," *Physical Review E* 101 (2020):052206.

83. S. Hari and F. R. Kschischang, "Bi-Directional Algorithm for Computing Discrete Spectral Amplitudes in the NFT," *Journal of Lightwave Technology* 34 (2016): 3529–3537.

84. V. Aref, "Control and Detection of Discrete Spectral Amplitudes in Nonlinear Fourier Spectrum," preprint, arxiv, 2016, https://doi.org/10.48550/arXiv.1605.06328.

85. P. J. Prins and S. Wahls, "Soliton Phase Shift Calculation for the Korteweg-de Vries Equation," *IEEE Access* 7 (2019): 122914–122930.

86. M. Kamalian Kopae, A. Vasylchenkova, D. Shepelsky, J. E. Prilepsky, and S. K. Turitsyn, "Full-Spectrum Periodic Nonlinear Fourier Transform Optical Communication Through Solving the Riemann-Hilbert Problem," *Journal of Lightwave Technology* 38, no. 14 (2020): 3602–3615.

87. G. Xiao and K. Yashiro, "An Efficient Algorithm for Solving Zakharov-Shabat Inverse Scattering Problem," *IEEE Transactions on Antennas and Propagation* 50 (2002): 807–811.

88. O. V. Belai, L. L. Frumin, E. V. Podivilov, and D. A. Shapiro, "Efficient Numerical Method of the Fiber Bragg Grating Synthesis," *Journal of the Optical Society of America B* 24 (2007): 1451–1457.

89. L. L. Frumin, O. V. Belai, E. V. Podivilov, and D. A. Shapiro, "Efficient Numerical Method for Solving the Direct Zakharov–Shabat Scattering Problem," *Journal of the Optical Society of America B* 32 (2015): 290–296.

90. S. B. Medvedev, I. A. Vaseva, and M. P. Fedoruk, "High-Order Block Toeplitz Inner-Bordering Method for Solving the Gelfand–Levitan–Marchenko Equation," *Communications in Nonlinear Science and Numerical Simulation* 138 (2024):108255.

91. S. Medvedev, I. Vaseva, and M. Fedoruk, "Fast Nonlinear Fourier Transform Algorithm for Reconstruction of Optical Data From Nonlinear Spectra of the Manakov System," *Optics Letters* 49 (2024): 4677–4680.

92. A. Rosenthal and M. Horowitz, "A New Inverse Scattering Algorithm for Reconstructing Highly Reflecting Fiber Bragg Gratings," *Conference on Quantum Electronics and Laser Science (QELS) - Technical Digest Series* 89 (2003): 1018–1026.

93. A. Rosenthal and M. Horowitz, "Inverse Scattering Algorithm for Reconstructing Strongly Reflecting Fiber Bragg Gratings," *IEEE Journal of Quantum Electronics* 39 (2003): 1018–1026.

94. F. Ahmad and M. Razzaghi, "A Numerical Solution to the Gel'fand-Levitan-Marchenko Equation," *Applied Mathematics and Computation* 89 (1998): 31–39.

95. S. Wahls and H. V. Poor, "Fast Inverse Nonlinear Fourier Transform for Generating Multi-Solitons in Optical Fiber," in *International Symposium on Information Theory (ISIT), Hong Kong* (IEEE, 2015), 1676–1680.

96. V. Vaibhav and S. Wahls, "Introducing the Fast Inverse NFT," in *2017 Optical Fiber Communications Conference and Exhibition (OFC)* (2017), 1–3.

97. V. Vaibhav, "Fast Inverse Nonlinear Fourier Transform," *Physical Review E* 98 (2018):013304.

98. S. Wahls and V. Vaibhav, "Fast Inverse Nonlinear Fourier Transforms for Continuous Spectra of Zakharov-Shabat Type," preprint, arxiv, 2016, https://doi.org/10.48550/arXiv.1607.01305.

99. V. Aref, S. T. Le, and H. Buelow, "Modulation Over Nonlinear Fourier Spectrum: Continuous and Discrete Spectrum," *Journal of Lightwave Technology* 36 (2018): 1289–1295.

100. S. Wahls, S. Chimmalgi, and P. J. Prins, "FNFT: A Software Library for Computing Nonlinear Fourier Transforms," *Journal of Open Source Software* 3 (2018): 597.

101. K. Onohara, T. Sugihara, Y. Miyata, et al., "Soft-Decision Forward Error Correction for 100 Gb/s Digital Coherent Systems," *Optical Fiber Technology* 17 (2011): 452–455.